remote sensing

MDPI

Article

Monitoring of Ionospheric Anomalies Using GNSS Observations to Detect Earthquake Precursors

Nicola Perfetti [1,2], Yuri Taddia [1,3] and Alberto Pellegrinelli [1,*]

[1] Engineering Department, University of Ferrara, 44122 Ferrara, Italy; nicola.perfetti@unife.it (N.P.); yuri.taddia@unife.it (A.P.)
[2] Topcon Positioning Italy, 60131 Ancona, Italy
[3] Consorzio di Bonifica Pianura di Ferrara, 44121 Ferrara, Italy
* Correspondence: alberto.pellegrinelli@unife.it

Abstract: The study of the Earth's ionosphere is a topic that has increased in relevance over the past few decades. The ability to predict the ionosphere's behavior, as well as to mitigate the effects of its rapid changes, is a matter of primary importance in satellite communications, positioning, and navigation applications at present. Ionosphere perturbations can be produced by geomagnetic storms correlated with the solar activity or by earthquakes, volcanic activities, and so on. The monitoring of space weather is achieved through analyzing the Vertical Total Electron Content (VTEC) and its anomalies by means of time series, maps, and other derived parameters. In this study, we outline a strategy to estimate the VTEC in real-time, its rate of change, and the corresponding Signal-to-Noise Ratio (SNR) based on dual-frequency GNSS Doppler observations. We describe how to compute these parameters from GNSS data for a regional network using Adjusted Spherical Harmonic Analysis (ASHA) applied to a local model. The proposed method was tested to study ionospheric anomalies for two seismic events: the 2015 Nepal and 2023 Turkey earthquakes. In both cases, anomalies were detected in the maps of the differential VTEC (DTEC), differential VTEC rate, and SNR of the VTEC produced close to the earthquake zone. The robustness of the results is strongly related to the availability of a dense Ionosphere Pierce Point (IPP) cloud on the ionospheric layer and surrounding the studied area. At present, the distribution of Continuously Operating Reference Stations (CORSs) around the world is insufficiently dense and homogeneous in certain regions (e.g., the oceans). Robustness can be improved by increasing the number of CORSs and developing new models involving measurements over ocean surfaces.

Keywords: GNSS; ionosphere; ionospheric anomalies; earthquake; TEC; VTEC; DTEC; SNR; space weather monitoring.

check for updates

Academic Editor: Yunbin Yuan

Received: 27 October 2024
Revised: 22 December 2024
Accepted: 24 December 2024
Published: 19 January 2025

Citation: Perfetti, N.; Taddia, Y.; Pellegrinelli, A. Monitoring of Ionospheric Anomalies Using GNSS Observations to Detect Earthquake Precursors. *Remote Sens.* **2025**, *17*, 338. https://doi.org/10.3390/rs17020338

Copyright: © 2025 by the authors. Licensee MDPI, Basel, Switzerland. This article is an open access article distributed under the terms and conditions of the Creative Commons Attribution (CC BY) license (https://creativecommons.org/licenses/by/4.0/).

1. Introduction

The ionosphere is a shell of ionized gas in the Earth's atmosphere which interacts with the Sun's fully ionized zone and the Earth's neutral region in a complex manner. It is a highly variable propagation medium capable of substantially influencing (i) radio communications [1], (ii) navigation [2,3], and (iii) remote sensing [4,5] technologies and applications, as well as playing an important role in space weather monitoring and forecasting [6,7]. The ionosphere impacts the technologies of GNSS communications in at least two ways, as (i) positioning and navigation applications are heavily affected by time delay errors induced by its charged particles and (ii), conversely, GNSS observations made

by Continuously Operating Reference Stations (CORSs) allow for the monitoring of the so-called ionospheric Total Electron Content (TEC) both spatially and temporally.

Ionospheric models have been developed to predict such errors. From the Klobuchar model, developed to support survey with single frequency receivers [8], to models used for precise real-time navigation and positioning applications with different satellite constellations [9,10], strategies have been set up for the Precise Point Positioning (PPP) of GNSS observations with the aim of mitigating the effects of ionospheric errors, especially in the estimation of GNSS ambiguities [11,12]. Conversely, from the point of view of space weather monitoring, it is important to detect ionosphere perturbations which can affect space-to-Earth radio communications, particularly for precise GNSS positioning and navigation applications and in situations where radio communications play a significant role in Safety of Life (SoL). Perturbations can be produced by geomagnetic storms strictly connected to the solar activity or due to local phenomena like earthquakes, volcanic ash emissions, huge desert storms, nuclear accidents, or tests. In the first case, they can be subdivided on the basis of their intensity into (i) large-scale storms, during which the enhancement of the solar wind energy generates perturbations at high latitudes that can influence the ionosphere globally and have high TEC variations (more than 200%); (ii) medium-scale Traveling Ionospheric Disturbances (TIDs) corresponding to TEC variations of a few TEC units (TECUs), for which the sources have not yet been comprehensively identified; and (iii) small-scale ionospheric perturbations correlated with steep TEC gradients [13]. Although ionosphere maps have been produced for many years both in post-processing [14,15] and in Near Real-Time (NRT) [16–18] applications, other projects and approaches have been developed focusing on monitoring and forecasting ionosphere perturbations. The Royal Observatory of Belgium uses a GNSS to produce the Vertical Total Electron Content (VTEC) in NRT for Europe, generating maps which are published every 15 minutes [19]. The processing strategy is based on L1 and L2 GNSS observations (from a network of permanent stations) used to retrieve the Slant TEC (STEC) from a geometry-free combination of phase-smoothed code observables. STEC values are biased by the Differential Code Bias (DCB) of satellites (DCB^s) and receivers (DCB_r) [20,21]: DCB^s are provided as products from International GNSS Service (IGS) Analysis Centers, while DCB_r are estimated using the a priori CODE [22] IONEX ionospheric model and RINEX data from the European Permanent Network (EPN) [23]. Monitoring space weather is crucial both for precision and for SoL GNSS applications. To improve the reliability of the results, processing strategies based on the estimation of spatial and temporal variations in TEC have been proposed and implemented. Spatial gradients and temporal variations computed starting from calibrated STEC measurements are translated in form of indices such as the Disturbance Ionosphere indeX (DIX), the Gradient Ionosphere indeX (GIXx, GIXy, and GIX), and the Sudden Ionosphere Disturbance indeX (SIDX) to obtain a clear and easily readable description of the level of perturbation of the ionosphere. The conciseness of these indices provides immediate and accessible information to GNSS users [24,25]. The Rate Of TEC (ROT) and Rate of TEC Index (ROT and ROTI), as time series or maps for monitoring the ionosphere during severe conditions, together with the scintillation index can be used to detect the size of irregularities between on a scale of hundreds of meters to kilometers [13,26–28].

Among the local sources of ionospheric perturbations, the most interesting and studied are certainly earthquakes. Ionospheric anomalies over earthquake preparation zones have been detected for many decades [29–31]. Anomalies consist of an increase or reduction in TEC around the epicenter starting from a few days to weeks before large earthquakes [32–36]. The main characteristics of an anomaly are of temporal and spatial nature and are closely related to the typical features of the precursor phenomena. The temporal parameters that characterize the anomaly are (i) the moment in which it occurs (with reference to the period

in which the earthquake occurs) and (ii) its duration. In general, the manifestation occurs in the 15 days preceding the event, with a duration that can vary from a few hours to 12 hours. Spatially, the anomaly is characterized by (i) the fact that its geographical position must overlap with the earthquake area; (ii) its altitude, which is aligned with that of the F-layer (F-region, although traces may also be present at other altitudes); and (iii) its extent, the order of magnitude of which is comparable with the radius of the earthquake preparation zone. Many earth–atmosphere and Earth–ionosphere coupling mechanisms have been proposed in the literature to explain the nature of these sources (critical argumentation can be found in Pulinets and Davidenko [36]): acoustic coupling mechanisms, Acoustic Gravity Waves, seismogenic electric fields, and electromagnetic coupling of the ground and ionosphere driven by electric currents and fields or by currents generated by charged aerosols. The pre-earthquake anomalies produce effects on the ionospheric potential (as well as the above-cited volcanic ash emissions, huge desert storms, nuclear accidents, and tests): the mechanism acts on the conductivity of the atmosphere, inducing variations in the ionospheric potential that can be detected using different observation techniques such as (i) vertical ionospheric sounding via ground-based ionosondes [32,37], (ii) vertical topside sounding from satellites [38], (iii) TEC monitoring via GNSS observations [19,33,39,40], (iv) low-orbit ionospheric tomography [41,42], and (v) the GNSS occultation technique [43]. Among these observations, those collected from GNSS receivers are widely used: TEC changes can be studied analyzing Global Ionosphere Maps (GIMs) produced by different centers such as CODE, ESA, and JPL [14] or computing them directly starting from the data collected by permanent GNSS stations [33,44]. The peculiarities of ionospheric TEC variations induced by an imminent seismic event are generally as follows:

1. Temporal variability occurs days before the main shock, usually in particular hours of day, with a certain duration;
2. Spatially speaking, the extent covers an area around the epicenter (with a symmetric manifestation in the opposite hemisphere due to the magnetically conjugated effect);
3. The seismic event induces an altitude distribution effect on the concentration of electrons.

All of these peculiarities hence provide a geometric interpretation of TEC variations from which it is possible to identify parameters to monitor, such as the following:

- The 15-day mean (or median) of the VTEC [36];
- The relative time series of the local VTEC;
- The geometry of VTEC anomalies, namely, their extent and position with respect to the epicenter;
- The vertical profile of the electron density [45].

As the technology evolves, the real-time monitoring of the ionosphere has become increasingly reliable. A database of parameters produced to monitor both space weather and ionosphere anomalies has been shared with a huge community of people.

In this paper, we propose a local model (i.e., using a limited number of CORSs located within a radius of thousands of kilometers from the epicenter instead of a global network) to estimate the following in real-time: (i) VTEC, (ii) its rate of change, and (iii) the relative Signal-to-Noise Ratio (SNR) based on dual-frequency GNSS Doppler observations. Receiver-to-satellite measurements are used to generate the geometry-free linear combination in which the VTEC, VTEC rate, and DCB rates are the parameters. Satellite DCB rates ($\dot{DCB}^s$) are computed using the data from IONEX files produced by global and local GNSS analysis centers, while receiver DCB rates (DCB_r) are, as a first approximation, considered as stochastic parameters. The novelty of this research consists of developing a procedure for the real-time estimation of both the VTEC and VTEC rate which can be used to compute useful parameters for monitoring ionospheric anomalies, even in

real-time. The rate of change in the VTEC is usually computed starting from the VTEC values themselves; in the present work, we detail a method for estimating them together, starting from GNSS observations. Two cases were investigated and analyzed: a first test was performed on the 2015 Nepal Mw 7.8 earthquake, whereas the second one concerned the 2023 Turkey Mw 7.8 earthquake. In both cases, real-time estimations of the VTEC, VTEC rate, and VTEC rate SNR series and maps were produced for a period of weeks before the earthquake event. A comparison between each variable and its 15-day mean was carried out for anomaly detection. The same investigation was performed using GIMs.

2. Materials and Methods

2.1. Model Implementation: From GNSS Doppler Observations to VTEC and VTEC Rate

GNSS Doppler measurements are the time derivatives of the carrier phase; thus, the corresponding observation equations contain time derivatives of geometric terms and biases. Ionospheric errors become functions of the TEC and TEC rate; at the same time, no ambiguity parameters need to be estimated since the equations contain only time derivatives of continuous variables. In order to implement a model based on Doppler observations for real-time estimation of ionospheric parameters, the following aspects need to be considered:

- Writing observation equations in terms of the VTEC and VTEC rate;
- Parameterizing the VTEC and VTEC rate as functions of latitude and longitude;
- Implementing the Kalman filter.

In the following, we analyze each of these aspects in detail.

2.1.1. Equations of GNSS Doppler Observations

A GNSS Doppler measurement is the rate of the phase observation. So, if we use j to identify carrier frequencies ($j = 1, 2$), r receivers, and s satellites, the Doppler observation at the time t is $D^s_{r,j}(t) = -\lambda_j \dot{\Phi}_j(t)$ [3,46,47], where $D^s_{r,j}(t)$ is the Doppler observation, $\dot{\Phi}_j(t)$ is the phase time derivative, and λ_j is the carrier wavelength. The corresponding observation equation is as follows:

$$D^s_{r,j}(t) = \dot{\rho}^s_{r,j}(t) + c\dot{\delta}^s_r(t) - \dot{I}^s_{r,j}(t) + \dot{T}^s_{r,j}(t) + c\left(\dot{\varepsilon}^s_j(t) + \dot{\varepsilon}_{r,j}(t)\right) + e^s_{r,j}(t). \quad (1)$$

In Equation (1), $\dot{\rho}^s_{r,j}(t)$ is the velocity of the range between the satellite and receiver, $\dot{\delta}^s_r(t)$ is the rate of the satellite–receiver clock error combination, $\dot{I}^s_{r,j}(t)$ and $\dot{T}^s_{r,j}(t)$ are the rates of the ionospheric and tropospheric terms, $\dot{\varepsilon}^s_j(t)$ and $\dot{\varepsilon}_{r,j}(t)$ are the rates of frequency-dependent satellite and receiver biases [48], and $e^s_{r,j}(t)$ is the noise term; all the terms are in m/s. The ionospheric error can be written as a function of VTEC and the zenith angle at the Ionosphere Pierce Point (IPP) z' : $I^s_{r,j}(t) = \frac{1}{\cos z'^s_r(t)} \frac{40.3}{f_j^2} VTEC(t)$, where f_j is the broadcasting carrier frequency in Hz, and VTEC is the vertical TEC in TECU (1 TECU = 10^{16} electrons per m^2.). The zenith angle depends on the height of the ionospheric layer h_m, the Earth radius R_e, and the zenith angle at the observation site $z^s_{0r}(t)$: $\sin z'^s_r(t) = \frac{R_e}{R_e + h_m} \sin z^s_{0r}(t)$ [46]. The corresponding time derivative is as follows:

$$\dot{I}^s_{r,j}(t) = \frac{\dot{z}'^s_r(t) \tan\left(z'^s_r(t)\right)}{\cos z'^s_r(t)} \frac{40.3}{f_j^2} VTEC(t) + \frac{1}{\cos z'^s_r(t)} \frac{40.3}{f_j^2} \dot{VTEC}(t), \quad (2)$$

where $\dot{z}'^s_r(t) = \frac{R_e}{R_e + h_m} \frac{\cos z^s_{0r}(t)}{\cos z'^s_r(t)} \dot{z}^s_{0r}(t)$ and $\dot{z}^s_{0r}(t) = \frac{\dot{r}^s_r(t) \cos z^s_{0r}(t) - \dot{u}^s_r(t)}{r^s_r(t) \sin z^s_{0r}(t)}$.

To compute $\dot{z}^s_{0r}(t)$, it is necessary to consider that, in the receiver local reference system, $z^s_{0r}(t)$ is the angle between the up axis and the receiver–satellite vector $r^s_r(t)$. The

up component of $r_r^s(t)$ is then $u_r^s(t) = r_r^s(t)\cos z_{0r}^s(t)$, where $r_r^s(t)$, $\dot{r}_r^s(t)$, $u_r^s(t)$, and $\dot{u}_r^s(t)$ are functions of the satellite position in the Earth-Centered, Earth-Fixed (ECEF) reference system. If we use broadcast orbits, the rates can be computed as described in Remondi [49]; if instead we start from precise orbits, Lagrange interpolation can be used to compute precise coordinates and then the corresponding rates via a numerical differentiation method (e.g., using a five-point formula [50]). To generate the geometry-free combination, we subtract L1 and L2 Doppler observations $D_{r,4}^s(t) = D_{r,1}^s(t) - D_{r,2}^s(t)$, and we introduce the rates of differential code biases [51,52] (inter-frequency biases) for the satellite and for the receiver, respectively, $D\dot{C}B^s(t) = \dot{\varepsilon}_1^s(t) - \dot{\varepsilon}_2^s(t)$ and $D\dot{C}B_r(t) = \dot{\varepsilon}_{r,1}(t) - \dot{\varepsilon}_{r,2}(t)$. At this stage, the observation equation is finally as follows:

$$\begin{aligned} D_{r,4}^s(t) = & \frac{40.3\left(f_1^2 - f_2^2\right)}{f_1^2 f_2^2 \cos z'^s_r(t)} \dot{z}'^s_r(t) \tan z'^s_r(t) VTEC(t) + \\ & + \frac{40.3\left(f_1^2 - f_2^2\right)}{f_1^2 f_2^2 \cos z'^s_r(t)} V\dot{T}EC(t) + c\left(D\dot{C}B_r(t) - D\dot{C}B^s(t)\right) + e_{r,4}^s(t). \end{aligned} \tag{3}$$

2.1.2. Parameterization of VTEC and VTEC Rate

$VTEC(t)$ and $V\dot{T}EC(t)$ are variables, functions of space (besides time), and hence to produce real-time estimation they have to be written as series of spherical harmonic functions depending on the latitude and longitude of IPPs [53]. Since we are interested in using a local model, namely, a spatially limited case, we record the expansion on a spherical cap by means of the Adjusted Spherical Harmonic Analysis (ASHA) [54,55]. Changing the domain of the expansion from the sphere to the cap means to define a new set of coordinates (the modified longitude and the colatitude), resulting in the following:

- The coordinates refer to a cap with the pole corresponding to the center of the region of interest;
- The colatitude θ is adjusted to θ' defined on a hemisphere $\theta' = s\theta$, with $s = {}^{90^\circ}/_{\theta_0}$ (θ_0 is the cap half-angle in degrees); now, the colatitude is defined in the interval $[0^\circ, 90^\circ]$;
- The Legendre functions in the new coordinates (longitude λ and colatitude θ') still have integer order and degrees.

The functions $VTEC$ and $V\dot{T}EC$ can be now written as follows:

$$VTEC(\lambda, \theta') = \sum_{k=0}^{K} \sum_{m=0}^{k} \left(g_k^m \cos m\lambda + h_k^m \sin m\lambda\right) P_k^m\left(\cos\theta'\right), \tag{4}$$

$$\begin{aligned} V\dot{T}EC(\lambda, \theta', \dot{\lambda}, \dot{\theta}') = \sum_{k=0}^{K} \sum_{m=0}^{k} \Big[& \left(\dot{g}_k^m \cos m\lambda + \dot{h}_k^m \sin m\lambda\right) P_k^m\left(\cos\theta'\right) \\ & + \left(-g_k^m \sin m\lambda + h_k^m \cos m\lambda\right) \dot{\lambda} P_k^m\left(\cos\theta'\right) \\ & + \left(g_k^m \cos m\lambda + h_k^m \sin m\lambda\right) \frac{\partial}{\partial t}\left(P_k^m\left(\cos\theta'\right)\right) \Big] \end{aligned} \tag{5}$$

where g_k^m and h_k^m are the estimable harmonic coefficients, $P_k^m(\cos\theta')$ are the corresponding Legendre functions of order m and degree k, and K is the degree at which the expansion is truncated. Now, the unknown parameters $VTEC(t)$ and $V\dot{T}EC(t)$ are replaced by the new unknowns g_k^m, $\dot{g}_k^m$, h_k^m, and $\dot{h}_k^m$.

2.1.3. Kalman Filter Implementation

At this point, the real-time knowledge of $VTEC(t)$ and $V\dot{T}EC(t)$ depends on the real-time estimation of the parameters g_k^m, $\dot{g}_k^m$, h_k^m, and $\dot{h}_k^m$ and on $D\dot{C}B_r(t)$ and $D\dot{C}B^s(t)$.

The first four types of variables are those actually involved in the estimation procedure; to test our model, we considered an expansion of order 10 and degree 8. $\dot{DCB}^s(t)$ can be instead computed using the $DCB^s(t)$ values in IONEX files [56]. To achieve this, we created series of these parameters, then we computed the derivative using a five-point formula for each of them. Finally, $\dot{DCB}_r(t)$ are considered as stochastic parameters; thus, their contributions were taken into account through the covariance matrix [57].

2.2. Model Products and Testing

The model described in Section 2.1 was tested to detect anomalies produced by earthquakes. In order to identify cases to be studied, besides the magnitude, we must consider the density of the CORSs surrounding the epicenter and within a radius of thousands of kilometers.

Finally, two cases were identified:

1. The Nepal earthquake of 2015:
   - magnitude: 7.8 Mww (Mww means Moment W-phase. The generic notation is Mw [58].);
   - Location: 28.231°N, 84.731°E;
   - Depth: 8.2 km;
   - Origin time: 25 April 2015 06:11:26 UTC (DOY 115).
2. The Turkey earthquake of 2023:
   - magnitude: 7.8 Mww (Mww means Moment W-phase. The generic notation is Mw [58].);
   - Location: 37.226°N, 37.014°E;
   - Depth: 10.0 km;
   - Origin time: 06 February 2023 01:17:34 UTC (DOY 37).

In both situations, we have a reasonable availability of permanent GNSS stations in certain areas, like Asia or Europe, in which they are homogeneously distributed, and conversely poor density on the sea and ocean surface as well as in the central part of Africa (where there are no active stations). This point is crucial since GNSS VTEC estimation is sensitive to the coverage of the IPPs over the area of interest. Inhomogeneous coverage can lead to negative VTEC value estimations during nighttime, and this is the case when a non-negligible part of the area of interest is covered by the ocean or is a territory without permanent GNSS stations [59].

Starting from the model outputs, it is possible to generate plots of both time series at a point of the ionospheric layer and/or maps (latitude–longitude) at a given time. In this work, we generated the following for the seismic events mentioned above:

- The time series of the VTEC in the epicenter;
- the time series of VTEC rate SNR in the epicenter (The SNR of the i-th element of an estimated parameter $\hat{p}$ with covariance matrix $Q_{\hat{p}}$ can be estimated as $\frac{\hat{p}_i}{\sigma_{p_i}}$.);
- The map of 24 h VTEC, that is, the time series of the VTEC in which the values are mapped with DOY on the x axis and the hour of the day on the y axis;
- The map of the 24 h VTEC rate SNR, that is, the time series of the VTEC rate SNR in which the values are mapped with DOY on the x axis and the hour of the day on the y axis;
- The maps of the differential VTEC, namely, the differential VTEC computed on every day with respect to the mean of the values of the previous 15 days, with a time step

of 1h (x axis: longitude; y axis: latitude). DTEC (or DVTEC), as well as the other differential quantities, is computed according to the formula

$$DTEC = 100 \cdot \frac{VTEC - \langle VTEC \rangle}{\langle VTEC \rangle}$$

where $\langle VTEC \rangle$ is the average value computed from 15 previous numerical values. VTEC is a function of latitude, longitude, and time, so in generating maps we compute DTEC starting from the VTEC of a specific day at a given hour and from the average values of VTEC for the same point of the previous 15 days at the same hour [60–62]. With reference to TEC, this approach is used to monitor the pattern of ionosphere parameter variations during the days before earthquakes. The corresponding maps allow to investigate the possible space-time correlation of the variation with the earthquake area and hour. In the past, it has been used for Nepal earthquake and also for earthquakes in Greece and Italy [61,63,64].;

- The maps of the VTEC rate SNR, with a time step of 1 h (x axis: longitude; y axis: latitude);
- The maps of the differential SNR (DSNR) of the VTEC rate, with a time step of 1 h (x axis: longitude; y axis: latitude).

In addition, we compared time series of the VTEC and maps of the DTEC with those from GIMs. The overall methodology adopted in this work is reported in Figure 1.

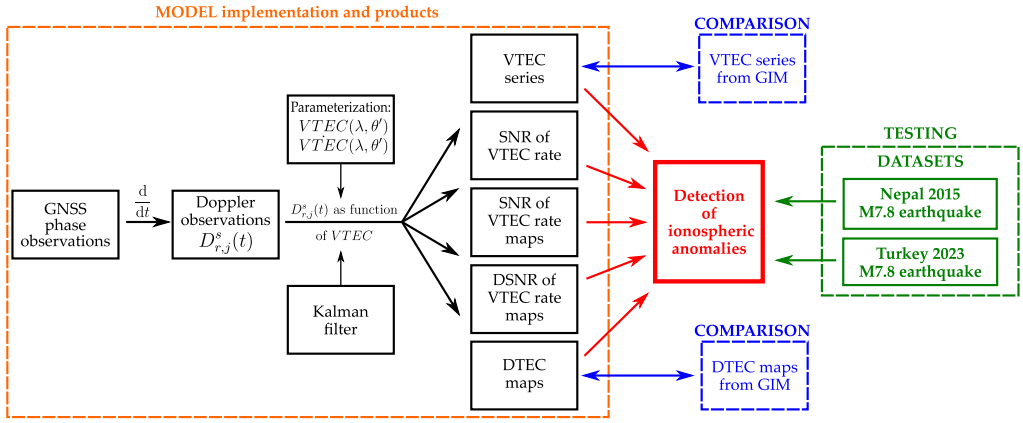


Figure 1. The methodology adopted in this work.

3. Results

3.1. Test of the Model Using the 2015 Nepal Mw 7.8 Earthquake

The earthquake occurred in Nepal on 25 April 2015, and some correlated coseismic ionospheric disturbances have already been discussed by many authors in the literature [65–67]; in this work, we investigated the ionosphere using the permanent GNSS network shown in Figure 2.

The network consists of 74 stations, 37 of which are double-constellation ones (i.e., GPS + Glonass). The stations are distributed in Asia, Africa, Australia, Europe, and the Antarctic region; some of them belong to networks in the Nepal region. Their data are available from the IGS [68–70], SONEL [71], UNAVCO [72], and CDDIS [73,74] databases. In order to increase the number of IPPs, we processed both GPS and Glonass data. We analyzed data from Day of Year (DOY) 81 to 115 of 2015 considering a cutoff angle of 12° and a ionospheric layer height of 450 km. The position of the center of the cap has a longitude of 94° and a latitude of 0°, while the cap amplitude is 108°. Finally, data were processed every 300 s.

Figure 3a shows the VTEC series computed at the epicenter point and compared with the VTEC gathered from GIMs. It is possible to see a few negative values due to (i) the fact that no constraints for VTEC values were introduced in the model and (ii) the absence of stations in the Indian Ocean. The mean difference between the computed VTEC values and those of the GIMs is about 20–25%. Possible reasons for such differences are (i) the fact that the network is local and rather small (there is a limited number of stations) if compared with the global one used to produce GIMs and (ii) that the order and the degree of the spherical expansion are different from those used for GIMs.

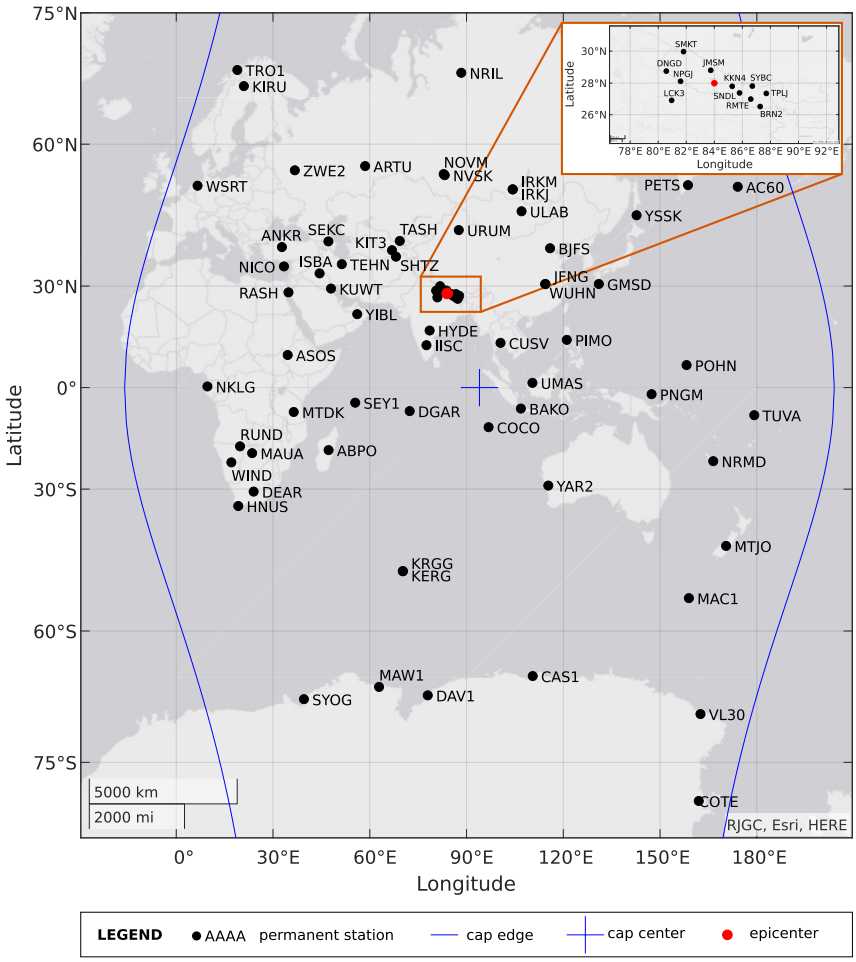


Figure 2. Distribution of the permanent GNSS stations used to study the Nepal earthquake. The cap edge, its center, and the projection of the epicenter are also shown.

We computed the SNR starting from the estimated VTEC rate values and their standard deviation. In Figure 4a, the VTEC rate SNR is superimposed on its 4-hour moving average: the SNR seems slightly increased in the period between DOYs 95 and 115 if compared with that of the previous 15 days. In Figures 3 and 4, the VTEC and VTEC rate SNR are also combined with the 24h map of their values (Figure 3b and Figure 4b, respectively) and finally compared to the plot of the geomagnetic activity index Kp (this index measures the energy of the solar wind impacting the Earth, and it is used by the space weather services in Near Real-Time [75]) reported in Figures 3c and 4c. All of these values were computed in the epicenter of the earthquake. Data on global geomagnetic activity were downloaded from the GFZ German Research Centre for Geosciences [76].

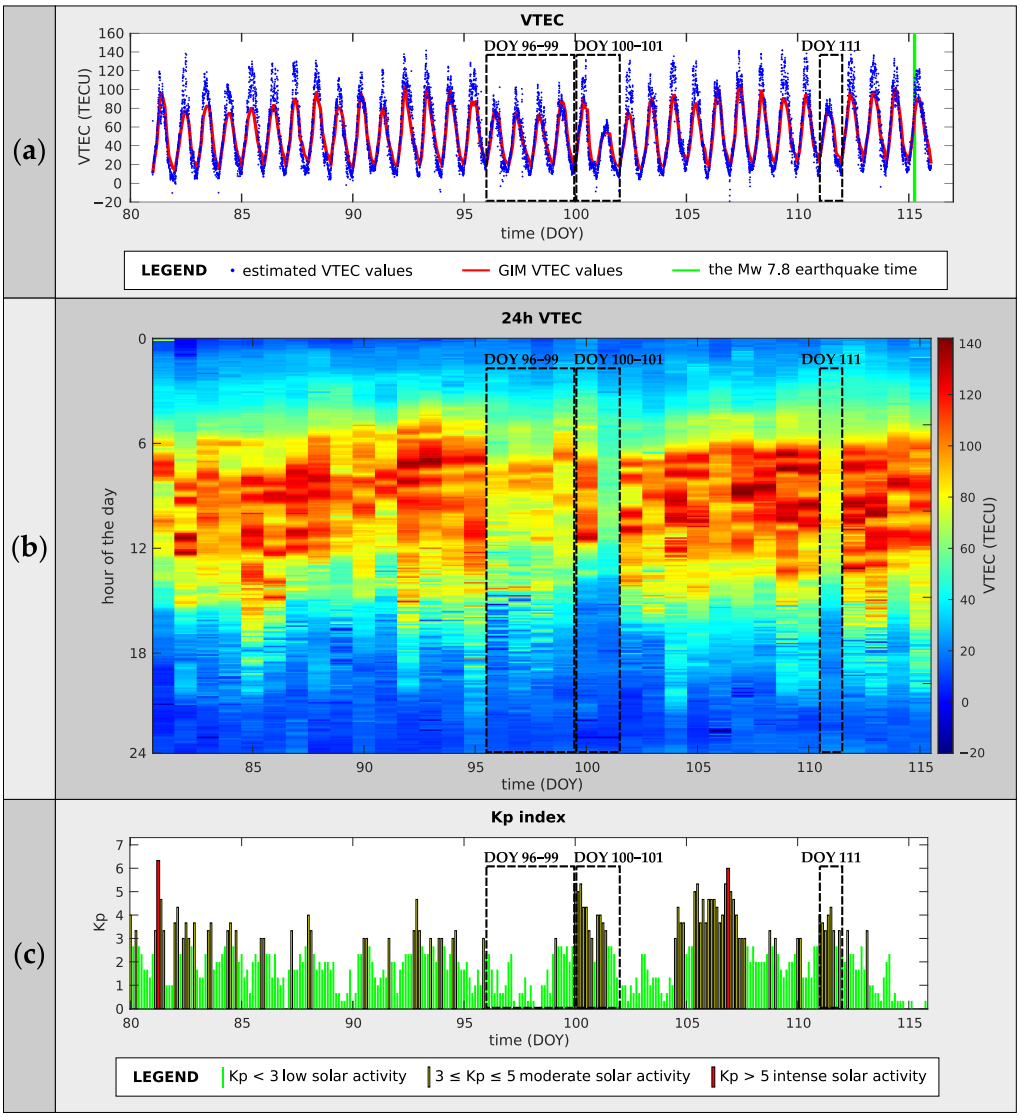


Figure 3. VTEC time series, 24 h VTEC, and Kp index for an overall comparison (all the values were computed at the epicenter of the Nepal earthquake): (**a**) VTEC time series of values estimated through the proposed model (blue dots) vs. GIM values (red line). The earthquake time is highlighted in green. Labels refer to midnight. (**b**) 24 h VTEC per DOY. Labels refer to midday. (**c**) The geomagnetic activity index Kp. Labels refer to midnight.

As a result, the VTEC seems to be influenced by the solar activity around DOYs 100–101. In this period, the values estimated through the proposed model and those deduced from GIMs are lower than the values of the other days. The same seems true for the low value of DOY 111. Furthermore, the high values of the VTEC rate SNR for DOYs from 101 to 107 seem to be correlated with the increased solar activity as shown by the Kp index, whereas those from DOYs 96 to 99 do not seem to be correlated with the solar activity. The analysis of the local VTEC and the local TEC rate SNR at the epicenter point hence does not give us any apparently useful information about ionospheric anomalies caused by the earthquake.

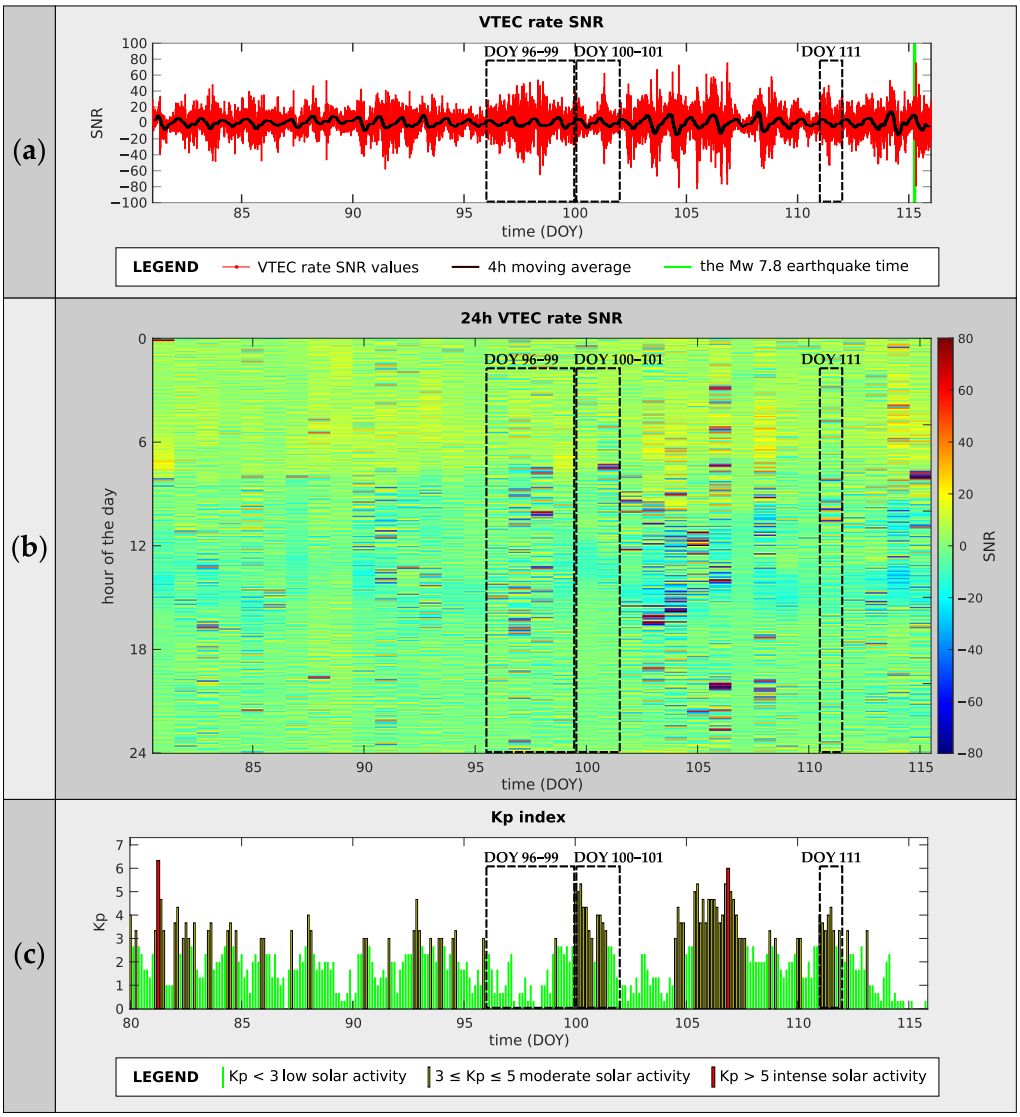


Figure 4. VTEC rate SNR time series, 24 h VTEC rate SNR, and Kp index for an overall comparison (all the values were computed at the epicenter of the Nepal earthquake): (**a**) VTEC rate SNR (red dot line) along with its 4 h moving average (black line). Labels refer to midnight. (**b**) 24 h VTEC rate SNR per DOY. Labels refer to midday. (**c**) The geomagnetic activity index Kp. Labels refer to midnight.

Considerably different findings were obtained from the analysis of maps. Figure 5 shows the DTEC maps computed using GIM values (Figure 5a) and VTEC estimated values (Figure 5b). Regarding DOY 111, Ouzounov et al. [66] report a negative anomaly in the DTEC map at 08 UT that is visible in Figure 5a. Despite a slightly different shape (and size) of the anomaly, the same is visible also in Figure 5b.

In Figure 6, we show the maps of the VTEC rate SNR at 03 UT (Figure 6a) and 08 UT (Figure 6b). In maps at 03 UT, anomalies over the earthquake zone appear for DOYs between 110 and 115 (the main shock was at 06:11 UT of DOY 115). Other anomalies also appear in DOYs 106 and 107, during which, however, there are high values of Kp that indicate an intense solar activity in such a time span. The same ionospheric anomalies are also visible in maps at 08 UT, in which that of DOY 111 is clearer here than in maps at 03 UT.

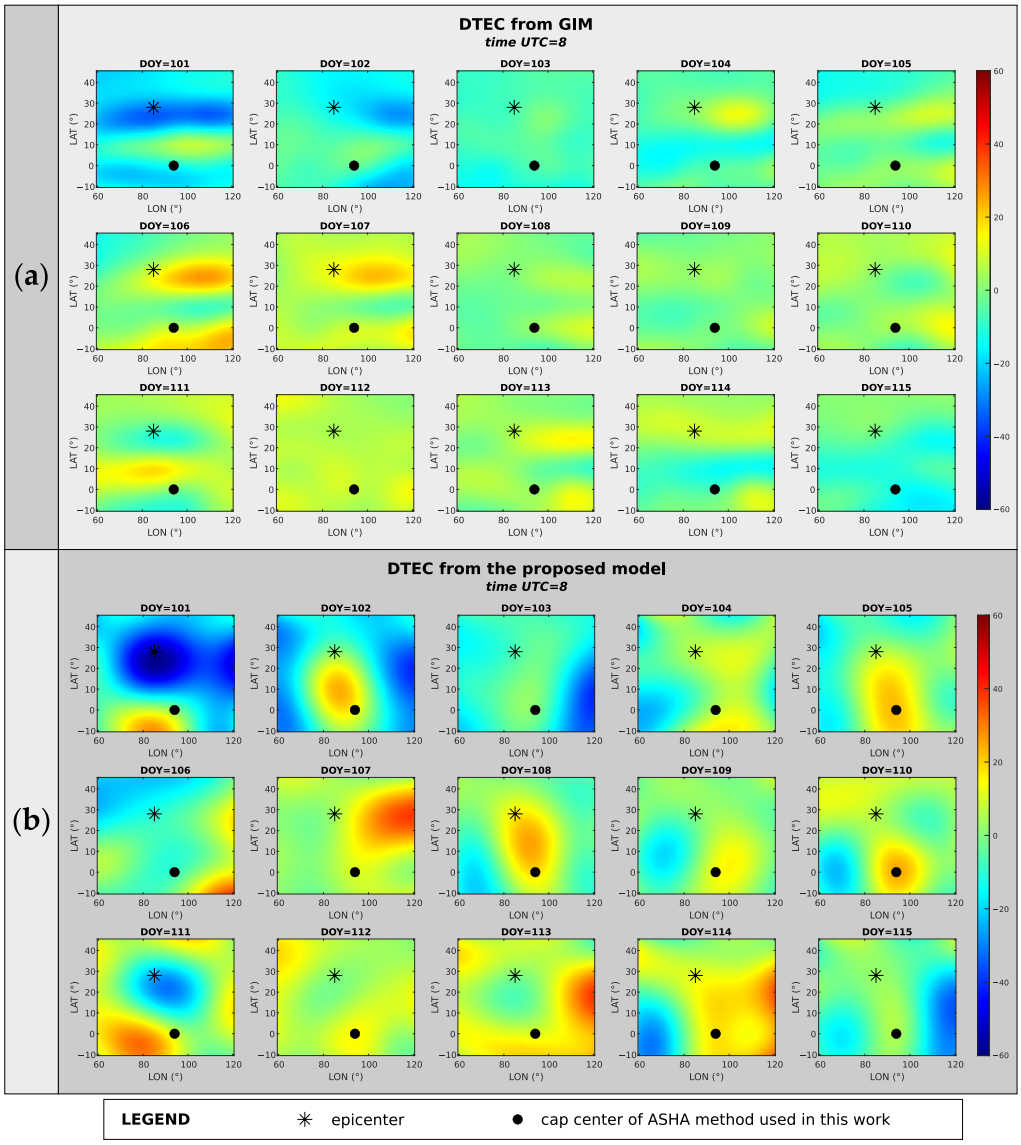


Figure 5. Maps of DTEC at 08 UT: (**a**) from GIMs; (**b**) from the proposed model.

3.2. Model Test Using the 2023 Turkey Mw 7.8 Earthquake

The second case examined in this work was the Mw 7.8 earthquake that occurred on 6 February 2023, in the southwestern region of Turkey, near the Turkey–Syria border. The network of GNSS stations used to investigate the presence of ionospheric anomalies is shown in Figure 7. The network consists of 55 IGS stations; 52 of them are double-constellation (GPS+Glonass), and the remaining 3 track only GPS signals (data retrieved from IGS, Sonel, UNAVCO, and CDDIS databases). In our analyses, we considered the period from DOYs 1 to 37 of 2023. A cutoff angle of 12° and a ionospheric layer height of 450 km were used. The position of the center of the cap has a longitude of 37° and a latitude of 37°, while the cap amplitude is 82°. Finally, data were processed every 300 s.

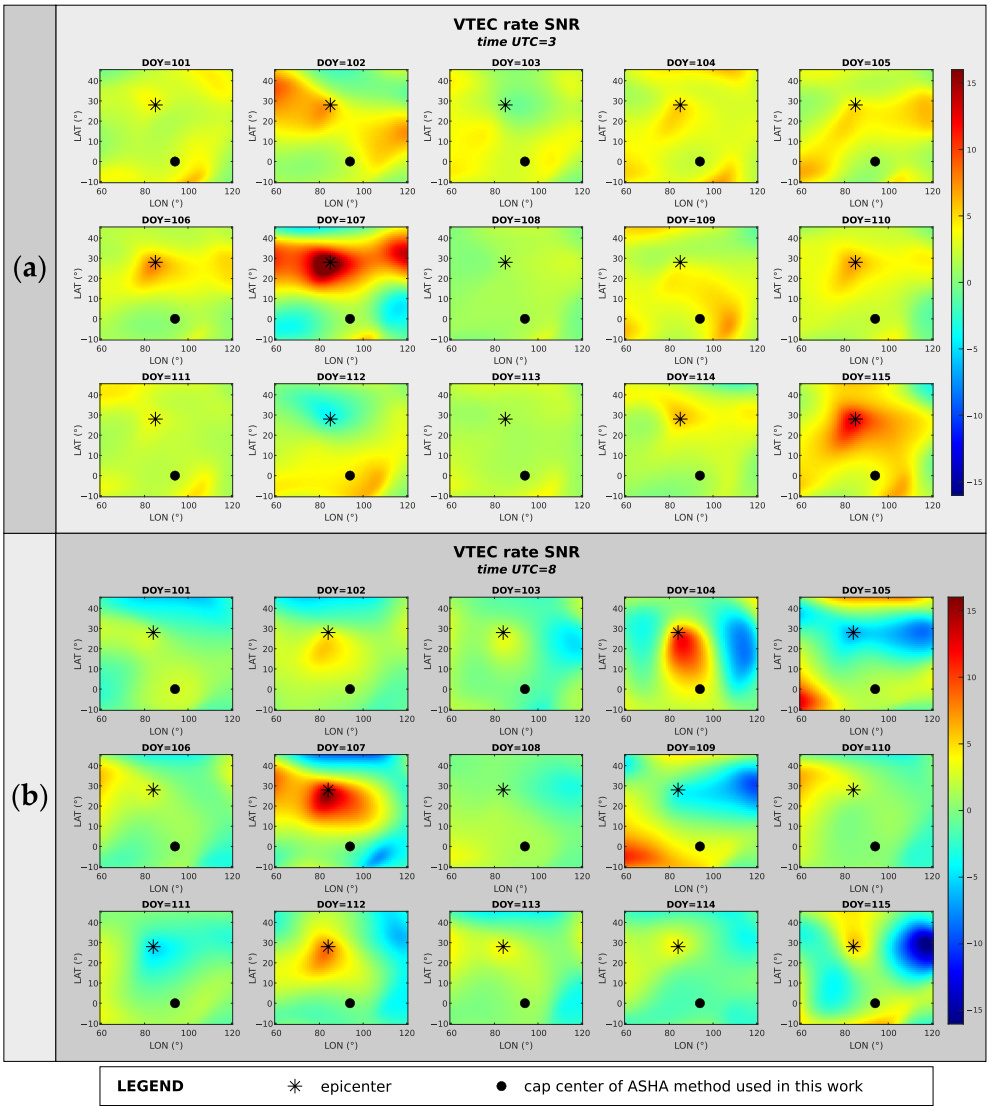


Figure 6. Maps of VTEC rate SNR: (**a**) at 03 UT; (**b**) at 08 UT.

Figure 8a shows the VTEC series computed at the epicenter point and compares it with the VTEC retrieved from GIMs. Also, in this case, it is possible to see a few negative values caused by the same factors discussed above. There are a small number of GNSS stations available within the central-northern region of Africa. The differences are slightly smaller than those reported in Section 3.1 and are around 15% here. The VTEC rate SNR, along with its own 4-hour moving average, is shown in Figure 9a. In this image, there are periods characterized by a higher noise level (as the moving average seems to report).

In Figures 8 and 9, the VTEC and VTEC rate SNR are also combined with the 24h map of their values (Figure 8b and Figure 9b, respectively) for each DOY (once again, computed in the epicenter of the earthquake) and finally compared with the plot of the geomagnetic activity index Kp reported in Figures 8c and 9c. Here, we can notice that (i) the high VTEC values in DOYs 15 and 18 correspond to a time span during which Kp values indicate an increased solar activity and (ii) for DOY 37, when the earthquake occurred, the VTEC value is high, especially in the central hours of the day, if compared with the days before. In the image of the 24h VTEC rate SNR, there are no visible effects of solar activity. In any case, the analysis of the local VTEC and the local VTEC rate SNR at the epicenter point does not produce any apparently substantial and definitive information about ionospheric anomalies.

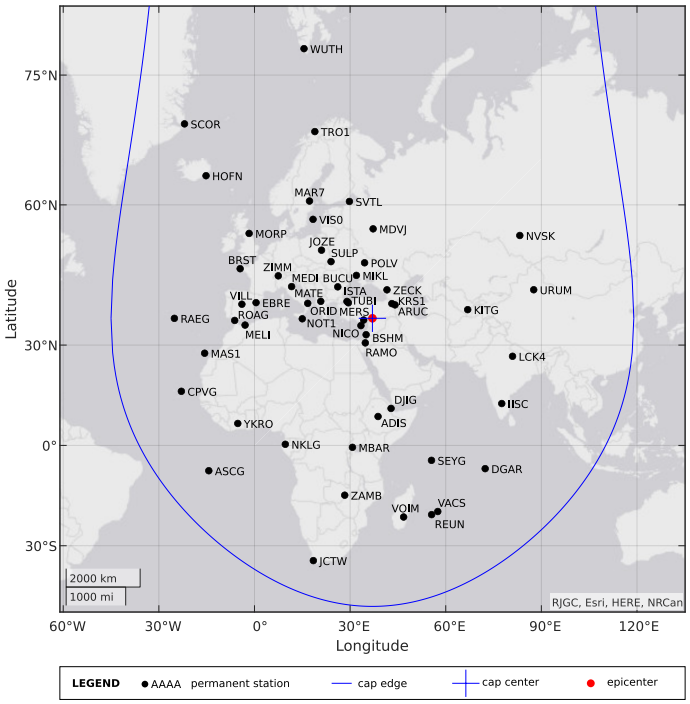


Figure 7. Distribution of the permanent GNSS stations used to study the Turkey earthquake. The cap edge, its center, and the projection of the epicenter are also shown.

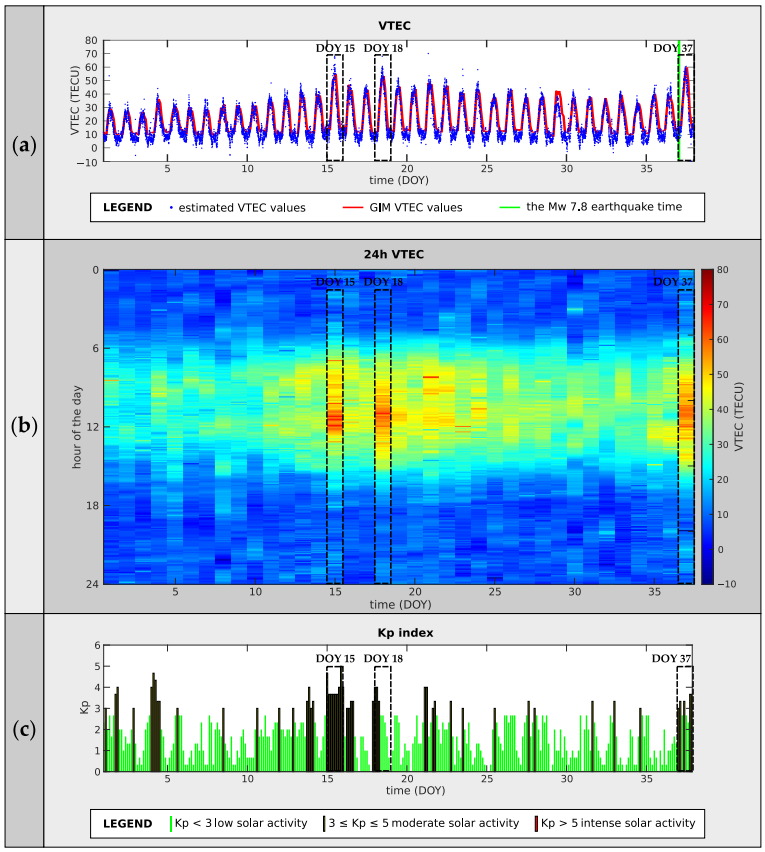


Figure 8. VTEC time series, 24 h VTEC, and Kp index for an overall comparison (all the values were computed at the epicenter of the Turkey earthquake): (**a**) VTEC time series of values estimated through the proposed model (blue dots) vs. GIM values (red line). The earthquake time is highlighted in green. Labels refer to midnight. (**b**) 24 h VTEC per DOY. Labels refer to midday. (**c**) The geomagnetic activity index Kp. Labels refer to midnight.

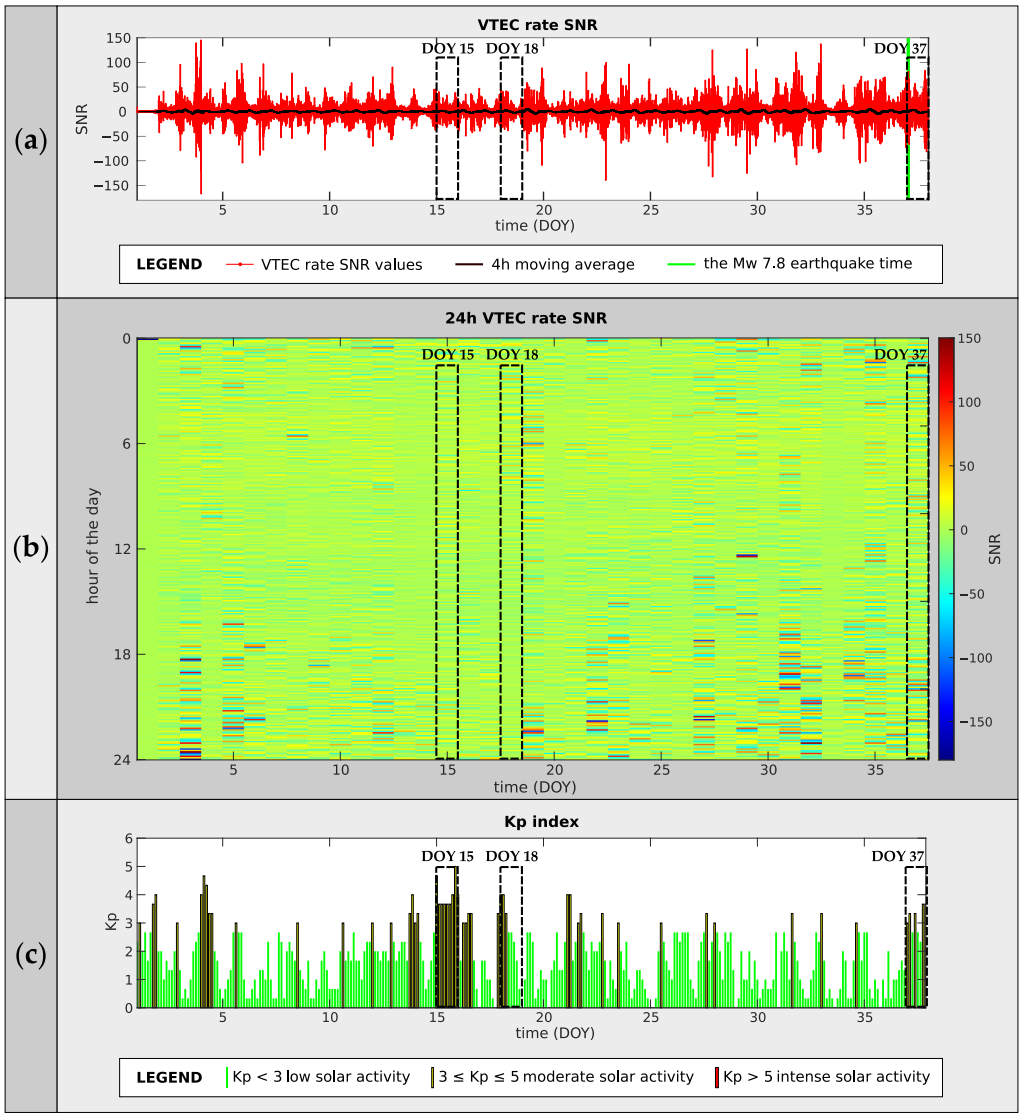


Figure 9. VTEC rate SNR time series, 24 h VTEC rate SNR, and Kp index for an overall comparison (all the values were computed at the epicenter of the Turkey earthquake): (**a**) VTEC rate SNR (red dot line) along with its 4 h moving average (black line). Labels refer to midnight. (**b**) 24 h VTEC rate SNR per DOY. Labels refer to midday. (**c**) The geomagnetic activity index Kp. Labels refer to midnight.

Figure 10a shows the DTEC maps derived from GIMs at 18 UT in which an anomaly with a duration of approximately 2 h is visible on DOY 29. Other anomalies, at the same hour, start from DOY 34, leading to the high DTEC values of the earthquake day (DOY 37). The DTEC derived using the proposed model (see Figure 10b) does not show the anomaly on DOY 29. An area of low DTEC is present over the epicenter site on DOY 31 (in this case with a duration of approximately 2 h), and from DOYs 34 to 37 high DTEC values characterize the same area. In this case, the maps of the VTEC rate SNR are not useful for investigating ionospheric anomalies. Conversely, by applying the idea of comparing the VTEC rate SNR with the mean of the previous 15 days, some interesting series appear at 17 UT (hence, one hour before) starting from DOYs 32 to 37. An area of low differential values and with an increasing extent appears over the earthquake zone (Figure 11). Furthermore, an anomaly of DTEC is also visible at 13 UT starting from DOY 18, both in the maps of the DTEC from GIMs and from the proposed model (Figure 12).

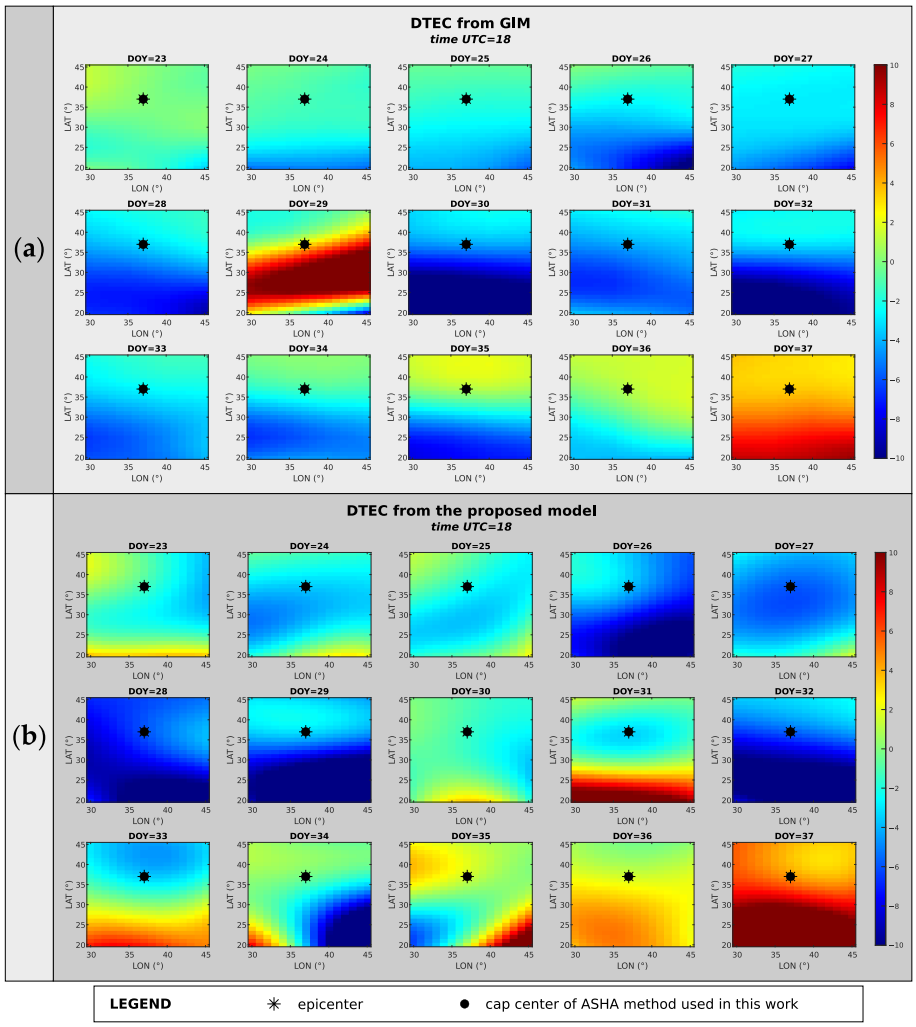


Figure 10. Maps of DTEC at 18 UT: (**a**) from GIMs, where anomalies of DTEC are visible starting from DOY 29; (**b**) from the proposed model.

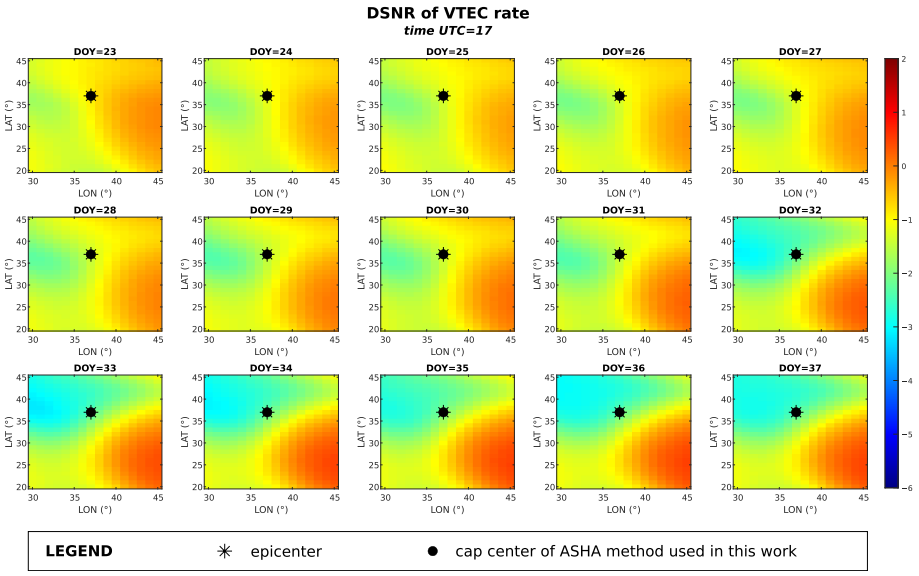


Figure 11. Maps of DSNR of VTEC rate at 17 UT from the proposed model.

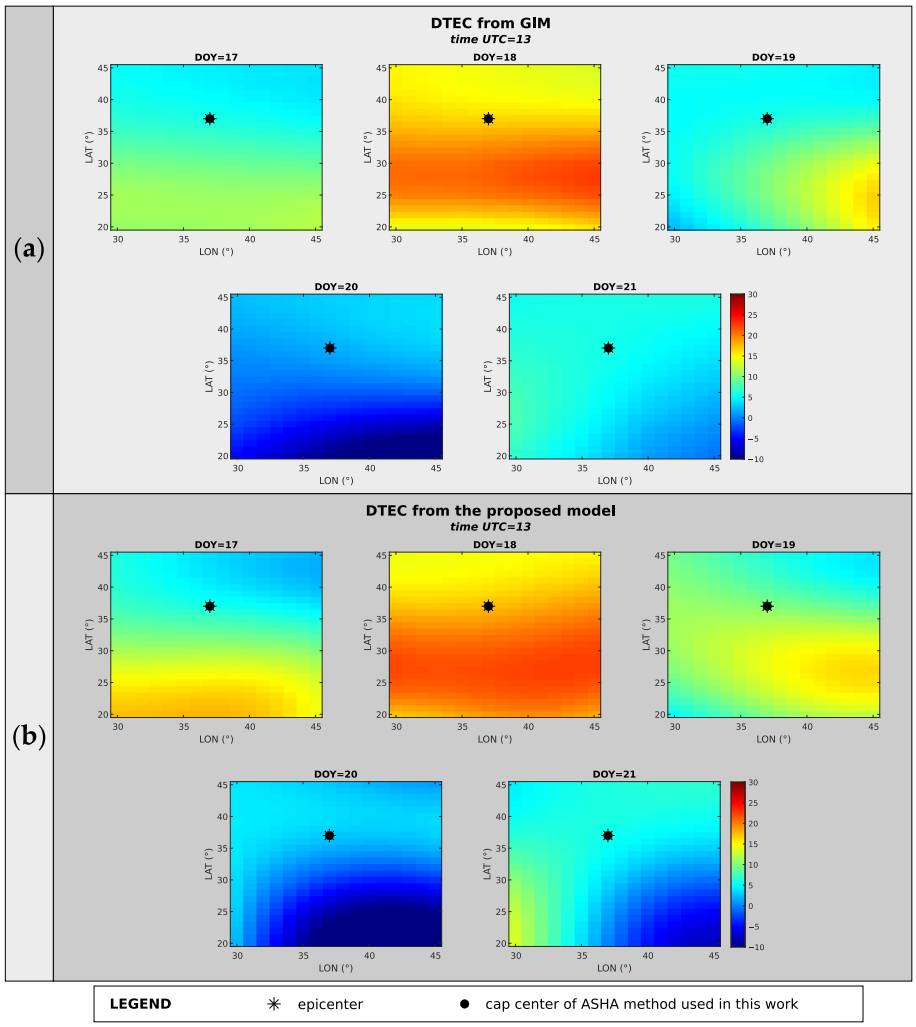


Figure 12. Maps of DTEC at 13 UT for DOYs 17 to 21: (**a**) from GIMs; (**b**) from the proposed model. Anomalies of DTEC are visible starting from DOY 18.

4. Discussion

In the cases studied, the proposed method allowed us to show possible anomalies correlated with geophysical events. Such a strategy is particularly interesting in ionosphere monitoring applications, considering that the results can be available in real-time. In the cases analyzed in this work, some possible tracks of ionospheric anomalies were detected in the maps of the DTEC, VTEC rate SNR, and DSNR of the VTEC rate over the earthquake zone. The anomalies have a duration of hours and started appearing between 7 and 10 days before the main shock. The radius of the preparation zone [36] in the earthquakes of the cases examined is approximately 2500 km (corresponding to approx. 20 degrees). The anomalies highlighted, in addition to being located positions corresponding to the earthquake zone, have an extent of tens of degrees, thus presenting characteristics compatible with those illustrated in Section 1.

The Nepal earthquake occurred in an epoch (DOY 115) close to the relative maximum of solar activity, for which local anomalies are superimposed on those induced by the solar wind. As presented in Section 3, in the 24h VTEC series plots (Figure 3), there are DOYs in which potential anomalies are characterized by low values of VTEC throughout the day. However, this is a condition that can only be investigated using maps. It is possible to identify anomalies during DOY 111 by mapping the 15-day differential values of real-time VTEC (both the estimated ones and those from GIMs). By means of the VTEC rate SNR maps, anomalies seem detectable starting from DOY 106. The use of maps allows us to

take into account the space(-time) correlation of the studied parameters, emphasizing their local nature, that is, their own dependence on local geophysical events. This, together with real-time estimation, provides us a tool for a quick detection. The same is true for the use of the SNR: in case of a local anomaly, the idea is that a bounded area should be affected by peculiar values of this parameter.

In the case of the Turkey earthquake (DOY 37), determining anomalies using a local model is slightly more difficult: the absence of permanent GNSS stations in the Africa region, especially in the central-northern area, together with the lack of stations in wide areas of Western Asia, makes it more difficult to estimate the VTEC and VTEC rate while avoiding border effects (no special constraints for the VTEC and VTEC rate are used at this level of the study). With the current GNSS CORS density and GNSS satellite constellations, the size of the anomaly we can detect is of the order of 1000 km. Whenever the density is insufficient or the distribution of the CORSs is not spatially homogeneous, the estimation can be affected by the above cited border effects, caused by the limited number of IPPs over these areas. This is particularly important in cases in which local models and real-time data processing are used for the investigation. Moreover, the earthquake occurred in 2023, a period in which the solar activity was increasing after the minimum reached in 2020. In Figure 8, we can see increasing values of 24h VTEC starting from DOY 10, with a minimum close to DOY 30, then the values finally increase again until the day of the earthquake. The solar activity may only partly explain this phenomenon. In this case, the maps of differential real-time VTEC show a single event, namely, a minimum DTEC on DOY 31 of a 2 h duration around 18 UT, whereas the GIM DTEC maps indicate a maximum during DOY 29 at 18 UT and an increasing value starting from DOY 35 over a wide area over the earthquake zone. A similar event is visible in the real-time DTEC on DOYs 36 and 37. The maps of the differential SNR of the VTEC rate in Figure 11 show a peculiar behavior over the earthquake area at 17 UT starting from DOY 32. The comparison between the current SNR map with the mean of the previous 15 days reveal a trend that is not visible using the maps of the simple VTEC rate SNR.

In Figure 8, high values of VTEC are present during DOYs 15 and 18; for DOY 15, this could be due to the recovery phase of the storm of DOYs 13 to 15, while for DOY 18 there does not seem to be a direct correlation with the solar activity. In Figure 12, the maps of DTEC from GIMs and from the proposed model at 13 UT show an increasing value during DOY 18 that can be read as an anomaly of a 2 hour duration. The lack of CORSs in the southern hemisphere prevents a deeper investigation into the events in this region and how they influenced the ionosphere over the earthquake area.

5. Conclusions

Space weather monitoring is presently a crucial activity supporting radio communications as well as navigation. Ionospheric anomalies are events which can significantly impact this task. One of the most important causes of the anomalies is the effect of the interaction between the solar activity and the magnetic activity; however, there is another cause of anomalies, which is correlated with notable geophysical events such as earthquakes.

To comprehensively determine space weather, it is important to detect these anomalies and, at the same time, to obtain information about the phenomena that produce them. GNSS observations are widely used for this scope, including GIMs and VTEC time series, as well as derived products like the DTEC, ROT, and ROTI, provide information about the ionosphere status. The processing of GNSS Doppler observations in real-time can give us other useful information to detect ionospheric anomalies. For this reason, the VTEC, VTEC rate, and VTEC rate SNR were produced in this work, and the analysis of their time series (for a specific point of the ionospheric layer), as well as their maps,

was used to detect ionospheric tracks of solar activity and tracks of interactions between Earth's magnetic field and the ground level in a geophysical active zone. As a result, some possible tracks of anomalies were detected. As the ionosphere is a dynamic system with a complex evolution in space and time, influenced and modified by causes of terrestrial and extraterrestrial origin, an anomaly can sometimes appear over areas that are not necessarily geologically active. Among all the possible anomalies revealed by maps, these overlapping geological faults should be considered first. The fact that anomalies can be detected in maps by referring to different parameters (DTEC, DSNR, etc.) can be lead to a strategy to identify those actually related to earthquakes. The anomalies correlated with the earthquake preparation phase can be identified by analyzing the values of different parameters (VTEC, DTEC, VTEC rate, SNR, etc.). A possible future development of the research will be to consider the possibility of cataloging the potential anomalies correlated with earthquakes on the basis of the values of these parameters, with the aim of verifying the presence of regularities in their manifestation.

Apart from the results obtained, it is necessary to remark that an increased number of CORSs is needed to improve the robustness of the model, primarily wherever the coverage of permanent stations is currently poor (e.g., Africa and some parts of Asia). This goal can be theoretically reached within the continents but not over the ocean surfaces, for which a different measurement technique (not necessarily involving GNSS stations) should perhaps be identified.

Author Contributions: Conceptualization, N.P.; methodology, N.P. and Y.T.; software, N.P. and Y.T.; validation, N.P.; formal analysis, N.P.; investigation, N.P., Y.T., and A.P.; resources, N.P. and A.P.; data curation, N.P.; writing—original draft preparation, N.P. and Y.T.; writing—review and editing, N.P. and Y.T.; visualization, N.P. and Y.T.; supervision, N.P.; project administration, A.P.; funding acquisition, A.P. All authors have read and agreed to the published version of the manuscript.

Funding: This research received no external funding.

Data Availability Statement: GNSS data used in this work are available on (i) the website of the International GNSS Service (IGS) https://igs.org/, (ii) the website of the Center for Orbit Determination in Europe of the Astronomical Institute of the University of Bern (CODE) http://ftp.aiub.unibe.ch/CODE/, (iii) the website of the Système d'Observation du Niveau des Eaux Littorales (SONEL) https://www.sonel.org/, (iv) the website of the University NAVSTAR Consortium (UNAVCO) https://www.unavco.org/, and (v) the website of the Crustal Dynamics Data Information System (CDDIS) https://cddis.nasa.gov/. Data on global geomagnetic activity are available on the website of the GFZ German Research Centre for Geosciences https://www.gfz-potsdam.de/en/.

Acknowledgments: GNSS data used in this work were provided by the International GNSS Service (IGS), the Center for Orbit Determination in Europe of the Astronomical Institute of the University of Bern (CODE), the Système d'Observation du Niveau des Eaux Littorales (SONEL), the University NAVSTAR Consortium (UNAVCO), and the Crustal Dynamics Data Information System (CDDIS). Data on global geomagnetic activity were downloaded from the GFZ German Research Centre for Geosciences.

Conflicts of Interest: The authors declare no conflicts of interest. The funders had no role in the design of the study; in the collection, analyses, or interpretation of data; in the writing of the manuscript; or in the decision to publish the results.

Abbreviations

The following abbreviations are used in this manuscript:

ASHA	Adjusted Spherical Harmonic Analysis
CDDIS	Crustal Dynamics Data Information System
CODE	Center for Orbit Determination in Europe of the Astronomical Institute of the University of Bern
CORS	Continuously Operating Reference Station
DCB	Differential Code Bias
DIX	Disturbance Ionosphere indeX
DOY	Day of Year
DTEC	Differential VTEC
ECEF	Earth-Centered, Earth-Fixed
EPN	European Permanent Network
ESA	European Space Agency
GIM	Global Ionosphere Map
GIX	Gradient Ionosphere indeX
GNSS	Global Navigation Satellite System
IGS	International GNSS Service
IONEX	IONosphere-map Exchange (format)
IPP	Ionosphere Pierce Point
JPL	Jet Propulsion Laboratory
NRT	Near Real-Time
PPP	Precise Positioning Processing
RINEX	Receiver INdependent EXchange (format)
ROT	Rate Of TEC
ROTI	Rate Of TEC Index
SIDX	Sudden Ionosphere Disturbance indeX
SNR	Signal-to-Noise Ratio
SoL	Safety of Life
SONEL	Système d'Observation du Niveau des Eaux Littorales
STEC	Slant TEC
TEC	Total Electron Content
TIDs	Traveling Ionospheric Disturbances
UNAVCO	University NAVSTAR Consortium
VTEC	Vertical TEC

References

1. Davies, K. *Ionospheric Radio*; Electromagnetics and Radar Series; Institution of Engineering & Technology: Stevenage, UK, 1990.
2. Kintner, P.M.; Kil, H.; Beach, T.L.; de Paula, E.R. Fading timescales associated with GPS signals and potential consequences. *Radio Sci.* **2001**, *36*, 731–743. [CrossRef]
3. Seeber, G. *Satellite Geodesy*; De Gruyter: Berlin, Germany; New York, NY, USA, 2003. [CrossRef]
4. Kutuza, B.; Bova, Y.; Kryukovsky, A.; Stasevich, V. Features of the Influence of the Earth's Ionosphere on the P-Band Propagation. In Proceedings of the EUSAR 2018; 12th European Conference on Synthetic Aperture Radar, Aachen, Germany, 4–7 June 2018; pp. 1–4.
5. Kryukovsky, A.S.; Bova, Y.I.; Kutuza, B.G.; Rastyagaev, D.V. Effects of Ionospheric Inhomogeneities on Remote Sensing of the Earth by Space-Borne P-Band SAR. *Radio Sci.* **2022**, *57*, e2021RS007341. [CrossRef]
6. Kelly, M. *The Earth's Ionosphere: Plasma Physics and Electrodynamics*; International Geophysics Series; Elsevier Science: Amsterdam, The Netherlands, 2012.
7. Jakowski, N. Ionosphere Monitoring. In *Springer Handbooks of Global Navigation Satellite Systems*; Springer: Berlin/Heidelberg, Germany, 2017; pp. 1139–1162. [CrossRef]
8. Klobuchar, J.A. Design and characteristics of the GPS ionospheric time delay algorithm for single frequency users. In Proceedings of the PLANS 1986—Position Location and Navigation Symposium, Las Vegas, NV, USA, 4–7 November 1986; pp. 280–286.
9. Hochegger, G.; Nava, B.; Radicella, S.; Leitinger, R. A family of ionospheric models for different uses. *Phys. Chem. Earth Part C Solar Terr. Planet. Sci.* **2000**, *25*, 307–310. [CrossRef]

10. Radicella, S.; Leitinger, R. The evolution of the DGR approach to model electron density profiles. *Adv. Space Res.* **2001**, *27*, 35–40. [CrossRef]
11. Dach, R.; Andritsch, F.; Arnold, D.; Bertone, S.; Fridez, P.; Jäggi, A.; Jean, Y.; Maier, A.; Mervart, L.; Meyer, U.; et al. *Bernese GNSS Software Version 5.2*; University of Bern, Bern Open Publishing: Bern, Switzerland, 2015. [CrossRef]
12. Wübbena, G.; Schmitz, M.; Bagge, A. PPP-RTK: Precise Point Positioning Using State-Space Representation in RTK Networks. In Proceedings of the ION GNSS, Long Beach, CA, USA, 13–16 September 2005; pp. 2584–2594.
13. Jakowski, N.; Béniguel, Y.; De Franceschi, G.; Pajares, M.H.; Jacobsen, K.S.; Stanislawska, I.; Tomasik, L.; Warnant, R.; Wautelet, G. Monitoring, tracking and forecasting ionospheric perturbations using GNSS techniques. *J. Space Weather. Space Clim.* **2012**, *2*, A22. [CrossRef]
14. Hernández-Pajares, M.; Juan, J.M.; Sanz, J.; Orus, R.; Garcia-Rigo, A.; Feltens, J.; Komjathy, A.; Schaer, S.C.; Krankowski, A. The IGS VTEC maps: A reliable source of ionospheric information since 1998. *J. Geod.* **2009**, *83*, 263–275. [CrossRef]
15. Crespon, F.; Jeansou, E.; Helbert, J.; Moreaux, G.; Lognonné, P.; Godet, P.; Garcia, R. SPECTRE (www.noveltis.fr/spectre): A web Service for Ionospheric Products. In Proceedings of the 1st Colloquium Scientific and Fundamental Aspects of the Galileo Program, Toulouse, France, 1–4 October 2007.
16. Mannucci, A.J.; Wilson, B.D.; Yuan, D.N.; Ho, C.H.; Lindqwister, U.J.; Runge, T.F. A global mapping technique for GPS-derived ionospheric total electron content measurements. *Radio Sci.* **1998**, *33*, 565–582. [CrossRef]
17. Fuller-Rowell, T.; Araujo-Pradere, E.; Minter, C.; Codrescu, M.; Spencer, P.; Robertson, D.; Jacobson, A.R. US-TEC: A new data assimilation product from the Space Environment Center characterizing the ionospheric total electron content using real-time GPS data. *Radio Sci.* **2006**, *41*, 1–8. [CrossRef]
18. Jakowski, N.; Mayer, C.; Hoque, M.M.; Wilken, V. Total electron content models and their use in ionosphere monitoring. *Radio Sci.* **2011**, *46*, 1–11. [CrossRef]
19. Bergeot, N.; Chevalier, J.M.; Bruyninx, C.; Pottiaux, E.; Aerts, W.; Baire, Q.; Legrand, J.; Defraigne, P.; Huang, W. Near real-time ionospheric monitoring over Europe at the Royal Observatory of Belgium using GNSS data. *J. Space Weather. Space Clim.* **2014**, *4*, A31. [CrossRef]
20. Coco, D.S.; Coker, C. Variability Of Gps Satellite Differential Group Delay Biases. *IEEE Trans. Aerosp. Electron. Syst.* **1991**, *27*, 931–938. [CrossRef]
21. Sardón, E.; Zarraoa, N. Estimation of total electron content using GPS data: How stable are the differential satellite and receiver instrumental biases? *Radio Sci.* **1997**, *32*, 1899–1910. [CrossRef]
22. Center for Orbit Determination in Europe of the Astronomical Institute of the University of Bern (CODE). CODE Website. Available online: http://ftp.aiub.unibe.ch/CODE/ (accessed on 1 September 2023).
23. Bruyninx, C.; Legrand, J.; Fabian, A.; Pottiaux, E. GNSS metadata and data validation in the EUREF Permanent Network. *GPS Solut.* **2019**, *23*, 106. [CrossRef]
24. Jakowski, N.; Borries, C.; Wilken, V. Introducing a disturbance ionosphere index. *Radio Sci.* **2012**, *47*, 1–9. [CrossRef]
25. Jakowski, N.; Hoque, M.M. Estimation of Spatial Gradients and Temporal Variations of the Total Electron Content Using Ground-Based GNSS Measurements. *Space Weather.* **2019**, *17*, 339–356. [CrossRef]
26. Wanninger, L. The occurrence of ionospheric disturbances above Japan and their effects on precise GPS positioning. In Proceedings of the CRCM 93, Kobe, Japan, 6–11 December 1993.
27. Pi, X.; Mannucci, A.; Lindqwister, U.; Ho, C. Monitoring of global ionospheric irregularities using the worldwide GPS network. *Geophys. Res. Lett.* **1997**, *24*, 2283–2286. [CrossRef]
28. Cherniak, I.; Zakharenkova, I.; Krankowski, A. IGS ROTI Maps: Current Status and Its Extension towards Equatorial Region and Southern Hemisphere. *Sensors* **2022**, *22*, 3748. [CrossRef]
29. Moore, G.W. Magnetic Disturbances preceding the 1964 Alaska Earthquake. *Nature* **1964**, *203*, 508–509. [CrossRef]
30. Davies, K.; Baker, D.M. Ionospheric effects observed around the time of the Alaskan earthquake of March 28, 1964. *J. Geophys. Res. (1896–1977)* **1965**, *70*, 2251–2253. [CrossRef]
31. Pulinets, S.; Boyarchuk, K. *Ionospheric Precursors of Earthquakes*; Springer: Berlin/Heidelberg, Germany, 2005; pp. 1–315. [CrossRef]
32. Liu, J.Y.; Chen, Y.I.; Chuo, Y.J.; Chen, C.S. A statistical investigation of preearthquake ionospheric anomaly. *J. Geophys. Res. Space Phys.* **2006**, *111*. [CrossRef]
33. Liu, J.Y.; Chuo, Y.J.; Shan, S.J.; Tsai, Y.B.; Chen, Y.I.; Pulinets, S.A.; Yu, S.B. Pre-earthquake ionospheric anomalies registered by continuous GPS TEC measurements. *Ann. Geophys.* **2004**, *22*, 1585–1593. [CrossRef]
34. Liu, J.Y.; Chen, Y.I.; Chuo, Y.J.; Tsai, H.F. Variations of ionospheric total electron content during the Chi-Chi Earthquake. *Geophys. Res. Lett.* **2001**, *28*, 1383–1386. [CrossRef]
35. Liu, J.Y.; Chen, Y.I.; Chen, C.H.; Liu, C.Y.; Chen, C.Y.; Nishihashi, M.; Li, J.Z.; Xia, Y.Q.; Oyama, K.I.; Hattori, K.; et al. Seismoionospheric GPS total electron content anomalies observed before the 12 May 2008 M7.9 Wenchuan earthquake. *J. Geophys. Res. Space Phys.* **2009**, *114*. [CrossRef]

36. Pulinets, S.; Davidenko, D. Ionospheric precursors of earthquakes and Global Electric Circuit. *Adv. Space Res.* **2014**, *53*, 709–723. [CrossRef]
37. Pulinets, S.; Liu, J.; Safronova, I. Interpretation of a statistical analysis of variations in the foF2 critical frequency before earthquakes based on data from Chung-Li ionospheric station (Taiwan). *Geomagn. Aeron.* **2004**, *44*, 102–106.
38. Pulinets, S.A.; Legen'ka, A.D. Spatial—Temporal Characteristics of Large Scale Disturbances of Electron Density Observed in the Ionospheric F-Region before Strong Earthquakes. *Cosm. Res.* **2003**, *41*, 221–230. [CrossRef]
39. Pulinets, S.A.; Bondur, V.G.; Tsidilina, M.N.; Gaponova, M.V. Verification of the concept of seismoionospheric coupling under quiet heliogeomagnetic conditions, using the Wenchuan (China) earthquake of May 12, 2008, as an example. *Geomagn. Aeron.* **2010**, *50*, 231–242. [CrossRef]
40. Belehaki, A.; Cander, L.; Zolesi, B.; Bremer, J.; Juren, C.; Stanisławska, I.; Dialetis, D.; Hatzopoulos, M. Ionospheric specification and forecasting based on observations from European ionosondes participating in DIAS project. *Acta Geophys.* **2007**, *55*, 398–409. [CrossRef]
41. Pulinets, S.; Romanov, A.; Urlichich, Y.; Doda, L.; Ouzounov, D. The first results of the pilot project on complex diagnosing earthquake precursors on Sakhalin. *Geomagn. Aeron.* **2009**, *49*, 115–123. [CrossRef]
42. Hirooka, S.; Hattori, K.; Nishihashi, M.; Takeda, T. Neural network based tomographic approach to detect earthquake-related ionospheric anomalies. *Nat. Hazards Earth Syst. Sci.* **2011**, *11*, 2341–2353. [CrossRef]
43. Chang, F.Y.; Liu, J.Y.; Chang, L.C.; Lin, C.H.; Chen, C.H. Three-dimensional electron density along the WSA and MSNA latitudes probed by FORMOSAT-3/COSMIC. *Earth, Planets Space* **2015**, *67*, 156. [CrossRef]
44. Padokhin, A.; Tereshin, N.; Yasyukevich, Y.; Andreeva, E.; Nazarenko, M.; Yasyukevich, A.; Kozlovtseva, E.; Kurbatov, G. Application of BDS-GEO for studying TEC variability in equatorial ionosphere on different time scales. *Adv. Space Res.* **2019**, *63*, 257–269. [CrossRef]
45. Smirnov, V. Solution of the inverse problem of electromagnetic transmission probing of the Earth ionosphere by gradient methods. *J. Commun. Technol. Electron.* **2001**, *41*, 41–45.
46. Hofmann-Wellenhof, B.; Lichtenegger, H.; Wasle, E. Observables. In *GNSS—Global Navigation Satellite Systems: GPS, GLONASS, Galileo, and More*; Springer: Vienna, Austria, 2008; pp. 105–160. [CrossRef]
47. Gurtner, W.; Estey, L. *RINEX—The Receiver Independent Exchange Format—Version 3.00*; University of Bern: Bern, Switzerland, 2007.
48. Leick, A. *GPS Satellite Surveying*; Wiley: Hoboken, NJ, USA, 2004.
49. Remondi, B.W. Computing satellite velocity using the broadcast ephemeris. *GPS Solut.* **2004**, *8*, 181–183. [CrossRef]
50. Burden, R.; Faires, J. *Numerical Analysis*; Cengage Learning: Boston, MA, USA, 2010.
51. Arikan, F.; Nayir, H.; Sezen, U.; Arikan, O. Estimation of single station interfrequency receiver bias using GPS-TEC. *Radio Sci.* **2008**, *43*. [CrossRef]
52. Wang, N.; Yuan, Y.; Li, Z.; Montenbruck, O.; Tan, B. Determination of differential code biases with multi-GNSS observations. *J. Geod.* **2016**, *90*, 209–228. [CrossRef]
53. Schaer, S. Mapping and predicting the Earth's ionosphere using the Global Positioning System. *Geodaetisch-Geophysikalische Arbeiten in der Schweiz*; Schweizerischen Geodätischen Kommission: Zurich, Switzerland, 1999; Volume 59.
54. De Santis, A. Conventional spherical harmonic analysis for regional modelling of the geomagnetic field. *Geophys. Res. Lett.* **1992**, *19*, 1065–1067. [CrossRef]
55. De Franceschi, G.; De Santis, A.; Pau, S. Ionospheric mapping by regional spherical harmonic analysis: New developments. *Adv. Space Res.* **1994**, *14*, 61–64. [CrossRef]
56. Schaer, S.; Gurtner, W.; Feltens, J. IONEX: The ionosphere map exchange format version 1. In Proceedings of the 1998 IGS Analysis Centers Workshop, Darmstadt, Germany, 9–11 February 1998.
57. Henderson, C.R.; Kempthorne, O.; Searle, S.R.; von Krosigk, C.M. The Estimation of Environmental and Genetic Trends from Records Subject to Culling. *Biometrics* **1959**, *15*, 192–218. [CrossRef]
58. U.S. Geological Survey. Magnitude Types. By Earthquake Hazards Program. Available online: https://www.usgs.gov/programs/earthquake-hazards/magnitude-types (accessed on 21 September 2024).
59. Zhang, H.; Xu, P.; Han, W.; Ge, M.; Shi, C. Eliminating negative VTEC in global ionosphere maps using inequality-constrained least squares. *Adv. Space Res.* **2013**, *51*, 988–1000. [CrossRef]
60. Pulinets, S.; Kotsarenko, A.; Ciraolo, L.; Pulinets, I. Special case of ionospheric day-to-day variability associated with earthquake preparation. *Adv. Space Res.* **2007**, *39*, 970–977. [CrossRef]
61. Pulinets, S.; Ouzounov, D. *The Possibility of Earthquake Forecasting*; 2053-2563, IOP Publishing: Bristol, UK, 2018. [CrossRef]
62. Pulinets, S.; Krankowski, A.; Hernandez-Pajares, M.; Marra, S.; Cherniak, I.; Zakharenkova, I.; Rothkaehl, H.; Kotulak, K.; Davidenko, D.; Blaszkiewicz, L.; et al. Ionosphere Sounding for Pre-seismic Anomalies Identification (INSPIRE): Results of the Project and Perspectives for the Short-Term Earthquake Forecast. *Front. Earth Sci.* **2021**, *9*, 610193. [CrossRef]

63. Davidenko, D.; Pulinets, S. Deterministic Variability of the Ionosphere on the Eve of Strong (M $\geq$ 6) Earthquakes in the Regions of Greece and Italy According to Long-Term Measurements Data. *Geomagn. Aeron.* **2019**, *59*, 493–508. [CrossRef]
64. Ouzounov, D.; Pulinets, S.; Davidenko, D.; Rozhnoi, A.; Solovieva, M.; Fedun, V.; Dwivedi, B.; Rybin, A.; Kafatos, M.; Taylor, P. Transient Effects in Atmosphere and Ionosphere Preceding the 2015 M7.8 and M7.3 Gorkha–Nepal Earthquakes. *Front. Earth Sci.* **2021**, *9*, 757358. [CrossRef]
65. Reddy, C.D.; Seemala, G.K. Two-mode ionospheric response and Rayleigh wave group velocity distribution reckoned from GPS measurement following Mw 7.8 Nepal earthquake on 25 April 2015. *J. Geophys. Res. Space Phys.* **2015**, *120*, 7049–7059. [CrossRef]
66. Ouzounov, D.; Pulinets, S.; Davidenko, D. Revealing pre-earthquake signatures in atmosphere and ionosphere associated with 2015 M7.8 and M7.3 events in Nepal. Preliminary results. *arXiv* **2015**, arXiv:1508.01805.
67. Chen, P.; Yao, Y.; Yao, W. On the coseismic ionospheric disturbances after the Nepal Mw7.8 earthquake on April 25, 2015 using GNSS observations. *Adv. Space Res.* **2017**, *59*, 103–113. [CrossRef]
68. International GNSS Service. IGS Website. Available online: https://igs.org/ (accessed on 1 September 2023).
69. Johnston, G.; Riddell, A.; Hausler, G. The International GNSS Service. In *Springer Handbook of Global Navigation Satellite Systems*; Springer International Publishing: Cham, Switzerland, 2017; pp. 967–982. [CrossRef]
70. Dow, J.M.; Neilan, R.E.; Rizos, C. The International GNSS Service in a changing landscape of Global Navigation Satellite Systems. *J. Geod.* **2009**, *83*, 191–198. [CrossRef]
71. Système d'Observation du Niveau des Eaux Littorales. SONEL Website. Available online: https://www.sonel.org/ (accessed on 1 September 2023).
72. University NAVSTAR Consortium. UNAVCO Website. Available online: https://www.unavco.org/ (accessed on 1 September 2023).
73. Crustal Dynamics Data Information System. CDDIS Website. Available online: https://cddis.nasa.gov/ (accessed on 1 September 2023).
74. Noll, C.E. The crustal dynamics data information system: A resource to support scientific analysis using space geodesy. *Adv. Space Res.* **2010**, *45*, 1421–1440. [CrossRef]
75. Bartels, J. III—The Geomagnetic Measures for the Time-Variations of Solar Corpuscular Radiation, Described for Use in Correlation Studies in Other Geophysical Fields. In *Geomagnetism*; Annals of The International Geophysical Year; International Council of Scientific Unions Comité Spécial de l'Année Géophysique Internationale (CSAGI), Ed.; Pergamon: London, UK, 2013; Volume 4, pp. 227–236. [CrossRef]
76. GFZ German Research Centre for Geosciences. GFZ Website. Available online: https://www.gfz-potsdam.de/en/ (accessed on 1 September 2023).

Disclaimer/Publisher's Note: The statements, opinions and data contained in all publications are solely those of the individual author(s) and contributor(s) and not of MDPI and/or the editor(s). MDPI and/or the editor(s) disclaim responsibility for any injury to people or property resulting from any ideas, methods, instructions or products referred to in the content.